Integrated predictive modeling of high-mode tokamak plasmas using a combination of core and pedestal models

Glenn Bateman, Miguel A. Bandrés, Thawatchai Onjun, Arnold H. Kritz, and Alexei Pankin
Department of Physics, Lehigh University, 16 Memorial Drive East, Bethlehem, Pennsylvania 18015

A new integrated modeling protocol is developed using a model for the temperature and density pedestal at the edge of high-mode (H-mode) plasmas [Onjun *et al.*, Phys. Plasmas **9**, 5018 (2002)] together with the Multi-Mode core transport model (MMM95) [Bateman *et al.*, Phys. Plasmas **5**, 1793 (1998)] in the BALDUR integrated modeling code to predict the temperature and density profiles of 33 H-mode discharges. The pedestal model is used to provide the boundary conditions in the simulations, once the heating power rises above the H-mode power threshold. Simulations are carried out for 20 discharges in the Joint European Torus and 13 discharges in the DIII-D tokamak. These discharges include systematic scans in normalized gyroradius, plasma pressure, collisionality, isotope mass, elongation, heating power, and plasma density. The average rms deviation between experimental data and the predicted profiles of temperature and density, normalized by central values, is found to be about 10%. It is found that the simulations tend to overpredict the temperature profiles in discharges with low heating power per plasma particle and to underpredict the temperature profiles in discharges with high heating power per particle. Variations of the pedestal model are used to test the sensitivity of the simulation results. © *2003 American Institute of Physics.* [DOI: 10.1063/1.1618234]

I. INTRODUCTION

During neutral beam heating experiments on the ASDEX tokamak in 1982, it was found that discharges with a sufficiently high heating power exhibit a spontaneous transition from a regime of confinement called low-mode (L-mode) to a regime with markedly improved confinement called high-mode (H-mode).[1] The change in the confinement is first apparent at the edge of the plasma, where a region of steep gradients in temperature and density is formed. This steep gradient region, which is called the pedestal, is caused by a transport barrier that forms near the edge of the plasma. The pedestal region is important because the height of the pedestal strongly influences the confinement of the core plasma.[2,3]

It has been found in integrated modeling simulations that the same core transport model used in simulations of L-mode dicharges can also be used in simulations of H-mode discharges, with equally good agreement with experimental data, as long as the simulation boundary conditions are given at the top of the pedestal at the edge of the H-mode discharges.[4] It has also been found in simulations of H-mode plasmas that the height of the pedestal has a large effect on the shape of the temperature and density profiles and, consequently, a large effect on the global confinement scaling.[4,5] However, the need to use experimental data to provide the temperatures and densities at the outer boundary of the integrated modeling simulations reduces the predictive capability of these simulations. Therefore, models are needed for the pedestal boundary conditions in order to make the integrated modeling simulations more predictive. It is important to develop more completely predictive integrated modeling codes in order to understand plasma confinement in present day

tokamaks and to predict the performance of new experiments and future fusion reactor designs such as ITER, FIRE, and IGNITOR.

Models that can be used to predict the temperature and density at the top of the pedestal have recently been developed and calibrated against experimental data.[6] In this paper, these predictive models for the pedestal at the edge of type I ELMy (edge-localized) H-mode tokamak plasmas[6] are combined together with predictive models for the core plasma[7] to produce integrated modeling simulations of existing tokamak experiments. The pedestal models were implemented in the BALDUR integrated modeling code[8] using an automated procedure to simulate the transition from the L-mode to H-mode, once the heating power rises above the H-mode threshold. When the plasma is in the H-mode state, the predicted values for the temperature and density at the top of the pedestal are used has boundary conditions in the simulations.

In previous BALDUR simulations of Ohmic, L-mode, and supershot discharges,[7,9,10] the Multi-Mode model was used in the plasma core out to the 97.5% flux surface which, typically, was the outermost flux surface that was available in the TRANSP analysis of experimental data. In those simulations, experimental data (or analyzed experimental data) were used as the boundary conditions. In previous simulations of H-mode discharges,[4,11] experimental data were used for the temperatures and density at the top of the pedestal to provide the boundary conditions in the BALDUR simulations, which are typically close to or outside of the 95% flux surface.

The combination of core and pedestal models used in this paper represents a step along the path to the more am-

4358   © 2003 American Institute of Physics

bitious goal of a complete theory in which flow shear and magnetic shear stabilize the turbulence that drives transport in the pedestal, while large scale instabilities produce periodic edge localized modes (ELMs). Alternative models for the H-mode pedestal have been implemented in the JETTO code[12] and ASTRA code.[13]

Thirty-three ELMy H-mode discharges, most of which are in the International Profile Database,[14] are simulated using the combination of predictive pedestal and core models in the BALDUR code.[8] Of the 33 H-mode discharges, 20 are taken from Joint European Torus (JET) experiments[15] and 13 are taken from DIII-D experiments.[16] The JET discharges include systematic scans of the normalized gyroradius (ρ_*), plasma pressure (β), collisionality (ν_*), gas fueling, and isotope mass. In addition, the simulation discharges include a discharge with 20% ^{3}He concentration, a high ρ_* discharge with large ELMs and a high β discharge, suitable for ITER scaling. The DIII-D discharges include systematic scans of ρ_*, β, elongation (κ), power, density (n_e), and a high performance discharge.

The simulation protocol, the transport models and the pedestal model used in this paper are described in Sec. II. Details of the experimental JET and DIII-D discharges are given in Sec. III. A statistical analysis of the temperature and density profiles produced by simulation, using the MMM95 and the pedestal model together, compared with experimental data, is presented in Sec. IV A. In addition, an analysis of the results is presented in this section. Conclusions are given in Sec. V.

II. SIMULATION PROTOCOL

All the simulations are carried out using the time dependent BALDUR integrated predictive modeling code (http://www.physics.lehigh.edu/baldur/index.htm).[8] The BALDUR transport code computes heat and particle sources (such as neutral beam injection heating), sinks (such as impurity radiation), transport fluxes, fusion reactions, magnetohydrodynamic equilibrium, and the effect of large-scale instabilities (such as sawtooth oscillations). The BALDUR transport code is used to compute the evolution of plasma profiles (such as temperature, density, and magnetic q profiles) given time-dependent boundary conditions (temperature, densities, equilibrium boundary shape). The transport model used in the BALDUR code is described in Sec. II A. The time dependent temperature and density boundary conditions in the H-mode state of the plasma were taken from the pedestal model described below in Sec. II B. The equilibrium boundary shape conditions are taken from the experimental data as a function of time. A description of the implementation of the pedestal model in the BALDUR code is presented in Sec. II C.

A. Transport model

The core transport model utilized in this paper is the MMM95 version of the Multi-Mode model, which is described in detail in Ref. 7. This model is available as a National Transport Code Collaboration (NTCC) computer code module at the website http://w3.pppl.gov/NTCC. The Multi-

Mode transport model is used to compute the total transport as a linear combination of transport driven by electrostatic drift modes, ideal magnetohydrodynamic (MHD) ballooning modes, and pressure-driven modes. Neoclassical transport is added to the anomalous transport computed using the Multi-Mode model. The MMM95 model is used to compute ion thermal, electron thermal, hydrogenic ion, and impurity ion particle transport channels self-consistently. Since the model is used in this paper without the effects of flow shear, the scaling of the model is completely gyro-Bohm (with diffusivities proportional to the speed of sound times the gyroradius squared).

The MMM95 version of the Multi-Mode model, which was developed in 1995, before flow shear became a commonly accepted paradigm, is a thoroughly tested and generally reliable core transport model. It was decided to use the MMM95 model without flow shear for the simulations of the conventional H-mode discharges in this paper because the MMM95 model without flow shear has been thoroughly tested in simulations of H-mode plasmas,[4,5,11] L-mode plasmas,[7,9,10] and other plasmas such as hot ion modes.[7] The simulations in this paper use the same core transport model that was used to simulate discharges in Ref. 4, where the pedestal temperatures and densities were taken from experimental data.

B. Pedestal model

A complete description of the pedestal model, based on magnetic and flow shear stabilization, that is used in this paper to predict the temperature at the top of the pedestal at the edge of the type 1 ELMy H-mode plasmas is given in Ref. 6. This pedestal model [which is referred to as model (1a) in Ref. 6] was chosen out of the six models presented in Ref. 6 because it produces the best agreement with experimental data for the temperature pedestal in JET and DIII-D, which are the tokamaks being simulated in this paper. The pedestal ion and electron temperatures are taken equal to the pedestal temperature predicted by this model.

In this model, the pressure gradient ($\partial p / \partial r$) within the pedestal region is assumed constant. The value of the temperature at the top of the H-mode pedestal, T_{ped}, is given by

$$T_{\text{ped}} = \frac{1}{2 k_B n_{\text{ped}}} \Delta \left| \frac{\partial p}{\partial r} \right|, \tag{1}$$

where n_{ped} is the density at the top of the pedestal, Δ is the pedestal width, k_B is the Boltzmann constant, and $|\partial p / \partial r|$ is ths pressure gradient, which is assumed to be uniform throughout the pedestal region. The width of the pedestal, Δ, is assumed to be determined by a combination of magnetic and flow shear stabilization of drift modes, $\Delta = C_W \rho s^2$, where C_W is a constant of proportionality, ρ is the ion gyroradius, and s is the magnetic shear. In this model, it is assumed that the pressure gradient is limited by the ballooning mode instability threshold, so that the normalized critical pedestal pressure gradient is given by

$$\alpha_c \equiv -\frac{2 \mu_o R q^2}{B_T^2} \left(\frac{\partial p}{\partial r} \right)_c = 0.4 s (1 + \kappa_{95}^2 (1 + 5 \delta_{95}^2)), \tag{2}$$

where the magnetic q and shear s are evaluated one pedestal width away form the separatrix [see Eq. (4) below] and B_T is the toroidal magnetic field. The dependence of α_c on elongation, κ_{95}, and triangularity, δ_{95}, at the 95% of the magnetic flux surface is described by the geometrical factor included in Eq. (2). Therefore the pedestal temperature takes the following form:

$$T_{\text{ped}}(\text{keV}) = 0.323 C_W^2 \left(\frac{B}{q^2}\right)^2 \left(\frac{M_i}{R^2}\right)\left(\frac{\alpha_c}{n_{\text{ped},19}}\right)^2 s^4, \tag{3}$$

where $n_{\text{ped},19}$ is the electron density at the top of the pedestal in units of 10^{19} m^{-3}, M_i is the ion mass, and R is the plasma major radius.

The magnetic q has a logarithmic singularity at the separatrix. At one pedestal width away from the separatrix, the magnetic q is approximated by

$$q = \left(\frac{0.85a^2 B}{I_{\text{MA}}R}\right)$$
$$\times \left(\frac{[1 + \kappa_{95}^2(1 + 2\delta_{95}^2 - 1.2\delta_{95}^3)](1.17 - 0.65a/R)}{[1 - (a/R)^2]^2}\right)$$
$$\times \left\{\left[1 + \left(\frac{r}{1.4a}\right)^2\right]^2 + 0.27\left|\ln\left(\frac{a-r}{a}\right)\right|\right\}, \tag{4}$$

where a is the minor radius of the separatrix, $r = a - \Delta$ is the minor radius at the top of the pedestal, and I_{MA} is the total plasma current in MA. Equation (4) is used to compute the magnetic q-value at the top of the pedestal, rather than using the q-value from an integrated modeling code or from measurements. Consequently, the pedestal temperature is computed in an isolated and self-consistent way in a stand-alone code or in an environment in which the details of the equilibrium and magnetic q profile are not available. In particular, the model is calibrated against experimental data in Ref. 6 using a stand-alone code in which the magnetic q is computed using Eq. (4). Hence, for consistency, Eq. (4) is used in the pedestal model even when values of the magnetic q are available from the integrated modeling code.

The magnetic shear, $s = (r/q)(\partial q/\partial r)$, which is computed using the magnetic q from Eq. (4), is then reduced by the effect of the bootstrap current, as described by Eqs. (36)–(41) in Ref. 6. Since the pedestal width is needed to compute the magnetic q, the magnetic shear, s, and the normalized pressure gradient, α_c, and since the pedestal width is a function of the pedestal temperature, the right-hand side of Eq. (3) for the pedestal temperature depends nonlinearly on the pedestal temperature. Consequently, an iterative nonlinear equation solver is used to solve Eq. (3) to determine T_{ped}.

The coefficient C_W in Eq. (3) was determined by calibrating the model for the pedestal temperature against 533 data points for type 1 ELMy H-mode plasmas obtained from the International Pedestal Database version 3.1 (http://pc-sql-server.ipp.mpg.de/Peddb) using discharges from ASDEX-U, DIII-D, JET, and JT-60U tokamaks. The value $C_W = 2.42$ yields a logarithmic rms deviation about 32%. The logarithmic rms deviation is defined as

$$\text{rms} = \sqrt{\frac{1}{N}\sum_{j=1}^{N}[\ln(T_{j,\text{ped}}^{\text{model}}/T_{j,\text{ped}}^{\text{experiment}})]^2}, \tag{5}$$

where $T_{j,\text{ped}}^{\text{model}}$ is the pedestal temperature predicted by the model, $T_{j,\text{ped}}^{\text{experiment}}$ is the experimentally measured pedestal temperature, and N is the number of tokamak discharges considered ($N = 533$). For the pedestal model referred to as the "standard" pedestal model, the value $C_W = 2.42$ is used. The sensitivity of the results to the choice of C_W will be examined in Sec. IV B.

The pedestal density is more constrained than the pedestal temperature, because the density profile is usually relatively flat in the core of H-mode discharges. Therefore, the pedestal density (n_{ped}) is a large fraction of the line averaged electron density ($\bar{n}_e$). The model for the density at the top of the pedestal used in this paper is a simple empirical expression $n_{\text{ped}} = 0.71\bar{n}_e$. It was found that this empirical expression fits the 533 data points with a logarithmic rms deviation of 12%.[17]

C. Implementation

In order to use predicted values for the temperature and density at the top of the pedestal as boundary conditions in the simulations, an automated H-mode procedure is used to simulate the transition from L-mode to H-mode.

This automated H-mode procedure changes the boundary conditions in the simulations from the experimental boundary conditions in L-mode to the predicted pedestal boundary conditions at the top of the pedestal in the H-mode state, when the heating power rises above the H-mode threshold. The power threshold for the H-mode is calculated using the following formula:[18]

$$P_{\text{L}\rightarrow\text{H}} = 2.84 M_i^{-1} B_T^{0.82} \bar{n}_{e20}^{0.58} R_m^{1.0} a_m^{0.81}[\text{MW}], \tag{6}$$

where M_i is the hydrogenic mass in amu, B_T is the vacuum toroidal magnetic field at major radius R along the flux surface in tesla, $\bar{n}_{e20}$ is the line average density in units of 10^{20} m^{-3}, R_m is the major radius in meters, and a_m the minor radius in meters.

Once the heating power rises above the H-mode threshold, the automated procedure makes a controlled spontaneous transition from the L-mode experimental boundary conditions to the predicted pedestal boundary conditions. In fact, this power threshold condition is met after the initiation of auxiliary heating in all of the discharges simulated in this paper. The time evolution of this transition is controlled in such way that it does not cause numerical instabilities in the BALDUR code. This automated H-mode procedure also controls the transition from H-mode back to L-mode when the heating power drops below 80% of the threshold power. ELMs are not included in the BALDUR simulations since a reliable model is not yet available in the BALDUR code for the frequency and radial extent of the ELMs. In addition, most of the experimental data available in the International Profile Database[14] does not resolve the time dependence of the periodic ELMs that are observed at the edge of the plasma. The temperature and density profiles predicted by

the simulations are compared with the corresponding experimentally measured profiles at a time slice that is late in the H-mode stage of each discharge.

The pedestal is generally more clearly defined in the density profile than it is in the temperature profiles. Consequently, the electron density profile was used to determine the minor radius of the plasma at the top of the pedestal. The cross-sectional shape of the plasma at the boundary of each simulation is taken from the observed shape of the plasma at the flux surface corresponding to the top of the pedestal. The minor radius at the boundary of each simulation, in particular, is a few centimeters smaller than the minor radius at the separatrix.

The input parameters used in the BALDUR simulation code during the H-mode stage of each discharge consists almost entirely of parameters that are controlled by the experimentalists. These input parameters include the plasma cross-sectional shape, the toroidal magnetic field strength, the plasma current, the line-averaged electron density (which is controlled by gas puffing in both the experiments and the simulations), and the characteristics of the neutral beam injection heating (i.e., power passing through the wall, energy of the neutral atoms, orientation and size of the beams). One of the BALDUR input parameters that is only indirectly controlled by experimentalists is the impurity concentration at the outer boundary of the simulation. The relative concentrations of the ion species are given as BALDUR input parameters as a function of time, while the electron density of the pedestal, which is predicted by the model described at the end of Sec. II B, is used to control the magnitudes of the ion densities at the outer boundary of each simulation.

III. H-MODE EXPERIMENTAL DATA

The experimental data from 29 of the H-mode discharges (16 JET, 13 DIII-D) considered in this paper were taken from the International Profile Database.[14] These data were processed by either the TRANSP code (http://w3.pppl.gov.transp) or the ONETWO code (http://fusion.gat.com/onetwo/), which are time-dependent transport analysis codes. In addition, four H-mode JET discharges were taken from the isotope scaling experimental dataset discussed in Refs. 11 and 19.

Major plasma parameters for the 33 discharges are listed in Tables I–VI. The following data are listed in each table: the major radius R (m) to the geometric center of the plasma; the minor radius a (m) or half-width at the top of the pedestal (the outer boundary of the simulation); the elongation κ, which is the vertical height of the plasma divided by the width of the plasma at the outer boundary of the simulation; the triangularity δ, which is the difference between R and the major radius of the top point on the outer boundary of the simulation divided by the minor radius a; the vacuum toroidal magnetic field B_T (T) at major radius R; the toroidal plasma current I_p (MA); the line-averaged electron density $\bar{n}_{e,19}$ in units of 10^{19} m^{-3}; the average Z_{eff}; the neutral beam injection (NBI) power passing through the wall of the tokamak P_{NB} (MW), which is not necessarily the absorbed power, and the power threshold for the transition

from L- to H-mode, $P_{L \rightarrow H}$ (MW), is computed using Eq. (6). The NBI energy, E_{NBI} (keV), is presented only in Table IV, since that energy varied significantly only in that one series of discharges with different hydrogenic isotope masses. The next variable, which will be used in the analysis presented in Sec. IV C, is proportional to the heating power per plasma particle $P_{heat}/(\bar{n}_{e,19}V)$, as it is computed in each of the standard simulations, where P_{heat} (MW) is the total heating power (Ohmic plus auxiliary), $\bar{n}_{e,19}$ is the line-averaged electron density in the simulation, and $V = 2\pi^2 R a^2 \kappa$ (m^3) is approximately the plasma volume out to the boundary of the simulation. The next three variables are pedestal variables, namely, the electron density $n_{e,19,ped}^{exp}$, the electron temperature $T_{e,ped}^{exp}$ (keV), and the ion temperature $T_{i,ped}^{exp}$ (keV) from experimental data at approximately the top of the pedestal. These are followed by the values of pedestal density and temperature, $n_{e,19,ped}^{sim}$ and T_{ped}^{sim} (keV), that are computed from the standard pedestal model as it is used in the simulations. The final item in each table is the diagnostic time, t_{diag} (s), during each discharge at which the simulation profiles are compared with the experimentally measured profiles.

Sections III A and III B below contain brief descriptions of each discharge.

A. JET discharges

The 20 JET ELMy H-mode discharges consist of three pairs of normalized gyroradius (ρ_*) scans, a β scan, a collisionallity (ν_*) scan, a gas fueling scan, four discharges in which the isotope mass was varied, an "identity" discharge, a high β discharge, a high ρ_* discharge, and a 20% ^{3}He discharge.

In the three pairs of normalized gyroradius scans, listed in Table I, ρ_* was varied by a factor of 1.6 while all other dimensionless parameters (q, ν_*, β) were held nearly fixed with an acceptable level of dimensionless similarity.[20,21] These discharges have various amplitudes, frequencies, and types of ELMS at the edge of the plasma. The JET discharges 35156, 35171 and 37944, 37379, comprise matched pairs that have heating power far above the H-mode power threshold. Experimental analysis indicates that the confinement follows a gyro-Bohm-type scaling, in agreement with ITER-93 scaling.[22] The other pair of discharges from the ρ_* scan, 33140 and 33131, have a heating power near the H-mode power threshold. The global energy confinement is observed to be between Bohm and stochastic.[21] All of these JET discharges were fueled with deuterium with the exception of the discharge 37944, which had a small 2% concentration of ^{3}He. The discharges were heated by neutral beam injection with the exception of the discharge 33131, which has an additional 1.7 MW of absorbed ion cyclotron resonance heating, which reduces to 10% of the NBI when the NBI heating is switched on.[14] The radio frequency power deposition profiles used in the BALDUR simulations are taken from the corresponding power deposition profiles in the International Profile Database.

The discharges 38407 and 38415, listed in Table II, are part of an ITER relevant β scan obtained using the Mark II

TABLE I. Plasma parameters for the JET gyroradius scan discharges.

Tokamak discharge type	JET 33131 Low ρ_*	JET 33140 High ρ_*	JET 35156 Low ρ_*	JET 35171 High ρ_*	JET 37944 Low ρ_*	JET 37379 High ρ_*
R (m)	2.94	2.93	2.86	2.88	2.89	2.91
a (m)	0.84	0.85	0.86	0.83	0.88	0.83
κ	1.70	1.56	1.56	1.58	1.72	1.62
δ	0.28	0.20	0.11	0.24	0.37	0.18
B_T (T)	3.06	1.74	2.18	1.09	2.60	1.05
I_p (MA)	2.83	1.61	2.05	1.01	2.58	0.97
$\bar{n}_{e,19}$	7.10	3.65	5.44	2.44	5.95	1.71
Z_{eff}	1.92	1.66	1.25	1.10	2.32	2.27
P_{NB} (MW)	18.0	5.80	8.60	2.91	11.6	3.70
$P_{\mathrm{L \to H}}$ (MW)	7.31	3.21	5.22	1.72	5.82	1.31
$P_{\mathrm{heat}}/(\bar{n}_{e,19}V)$	0.042	0.027	0.022	0.031	0.027	0.037
$n_{e,19,\mathrm{ped}}^{\mathrm{exp}}$	4.70	2.88	4.60	1.81	5.00	1.31
$T_{e,\mathrm{ped}}^{\mathrm{exp}}$ (keV)	1.47	0.96	2.78	0.61	1.73	0.80
$T_{i,\mathrm{ped}}^{\mathrm{exp}}$ (keV)	1.69	0.96	2.40	0.61	1.70	1.02
$n_{e,19,\mathrm{ped}}^{\mathrm{sim}}$	5.20	2.63	4.34	1.78	4.24	1.29
$T_{\mathrm{ped}}^{\mathrm{sim}}$ (keV)	1.49	1.20	0.95	0.78	1.33	1.08
t_{diag} (s)	55.69	56.50	55.85	65	60.14	63.39

divertor configuration.[14] In this scan, β was varied by a factor of 1.5 while holding ρ_*, ν_*, and magnetic q fixed. These plasmas contain 20% and 8% concentrations of ^{3}He, respectively. The pair of dimensionless scans, discharges 37728 and 37718, correspond to a ν_* scan. In this scan, the dimensionless collisionality was varied by a factor of 2.6 while holding ρ_* and β fixed.[5] The plasmas contain 7% and 18% concentrations of helium, respectively. Discharge 37728 was heated with the 1.1 MW of absorbed ion cyclotron frequency resonance heating in addition to 13.3 MW of neutral beam injected power. The pair of JET discharges, 38287 and 38285, are taken from a scan in which the gas fueling was varied at fixed beam power.[23] These discharges are dominantly NBI heated, but with 20% rf heating.

The JET discharges listed in Table III include discharge 32745, which was part of a divertor study[24] with 20% con-

centration of ^{3}He, discharge 35174, which has high ρ_* and large ELMs, and the high β discharge, 34340, which is suitable for ITER scaling. Also included in Table III is the ''identity discharge,'' JET 33465, which is part of a series of experiments designed to test ρ_* scaling among different tokamaks.

Finally, the four discharges listed in Table IV are ELMy H-mode JET discharges in which different hydrogenic isotopes—hydrogen, deuterium, or tritium—were used to fuel the plasma discharge and the neutral beam injected gas.[11]

Some of the discharges had irregularities complicating their study. For example, no information is available in the International Profile Database for the T_i profile of JET discharges 33140, 33465, 34340, 35171, and 35174. The T_i

TABLE II. Plasma parameters for the JET β, ν_*, and gas fueling scan discharges.

Tokamak discharge type	JET 37728 Low ν_*	JET 37718 High ν_*	JET 38287 Low gas	JET 38285 High gas	JET 38407 Low β	JET 38415 High β
R (m)	2.92	2.94	2.90	2.89	2.91	2.88
a (m)	0.87	0.87	0.84	0.90	0.86	0.88
κ	1.55	1.58	1.64	1.61	1.60	1.55
δ	0.20	0.12	0.19	0.19	0.16	0.11
B_T (T)	2.71	2.11	2.57	2.58	1.59	1.84
I_p (MA)	2.57	1.97	2.57	2.56	1.47	1.67
$\bar{n}_{e,19}$	4.90	4.54	5.72	6.57	3.05	4.02
Z_{eff}	1.76	1.93	1.85	1.92	2.09	2.06
P_{NB} (MW)	13.3	9.7	11.3	11.5	5.60	15.7
$P_{\mathrm{L \to H}}$ (MW)	5.56	4.05	5.35	6.37	2.63	3,75
$P_{\mathrm{heat}}/(\bar{n}_{e,19}V)$	0.038	0.035	0.033	0.025	0.027	0.054
$n_{e,19,\mathrm{ped}}^{\mathrm{exp}}$	3.85	3.31	4.48	4.36	2.39	3.02
$T_{e,\mathrm{ped}}^{\mathrm{exp}}$ (keV)	1.78	0.82	1.85	1.04	0.87	1.25
$T_{i,\mathrm{ped}}^{\mathrm{exp}}$ (keV)	1.64	1.09	1.80	1.02	1.04	1.35
$n_{e,19,\mathrm{ped}}^{\mathrm{sim}}$	3.72	3.09	3.94	4.82	2.23	3.19
$T_{\mathrm{ped}}^{\mathrm{sim}}$ (keV)	1.75	1.31	1.72	1.10	1.11	0.89
t_{diag} (s)	58.12	55.38	56.61	58.39	57.40	56.61

TABLE III. Plasma parameters for miscellaneous JET discharges.

Tokamak discharge type	JET 32745 D–He	JET 33465 Indentity	JET 34340 High β	JET 35174 High ρ_*
R (m)	2.87	2.87	2.87	2.87
a (m)	0.83	0.87	0.80	0.82
κ	1.69	1.55	1.66	1.56
δ	0.18	0.19	0.15	0.22
B_T (T)	2.96	1.08	2.16	1.08
I_p (MA)	3.04	1.04	2.03	1.02
$\bar{n}_{e,19}$	7.34	3.26	5.54	2.49
Z_{eff}	1.64	1.52	1.99	1.48
P_{NB} (MW)	16.2	2.77	17.7	6.92
$P_{\text{L}\rightarrow\text{H}}$ (MW)	6.19	2.02	4.36	1.57
$P_{\text{heat}}/(\bar{n}_{e,19}V)$	0.036	0.015	0.065	0.052
$n_{e,19,\text{ped}}^{\text{exp}}$	3.50	2.20	4.27	1.80
$T_{e,\text{ped}}^{\text{exp}}$ (keV)	1.30	0.52	1.08	0.81
$T_{i,\text{ped}}^{\text{exp}}$ (keV)	1.70	0.52	1.24	0.81
$n_{e,19,\text{ped}}^{\text{sim}}$	5.10	2.30	3.88	1.71
$T_{\text{ped}}^{\text{sim}}$ (keV)	1.66	0.58	1.32	0.92
t_{diag} (s)	56.44	63.76	56.37	64.38

profile data are set equal to T_e profile data for these discharges in the database. As a result, the ion temperature profiles for these discharges are not used in the statistical analysis presented in Sec. IV. In addition, the diagnostic time of 65.87 s given in the International Profile Database for JET 35171 occurred after the beam heating power was turned off. To correct this, the diagnostic time was chosen at a relatively steady state period of the core discharge, 65.0 s.[4] The diagnostic times for the other discharges are taken during quasi-stationary phases of each discharge at the time indicated in the International Profile Database.

TABLE IV. Plasma parameters for the JET isotope scan discharges.

Tokamak discharge type	JET 42794 Tritium Isotope	JET 42997 Tritium Isotope	JET 43134 Deuterium Isotope	JET 43452 Hydrogen Isotope
R (m)	2.95	2.95	2.95	2.95
a (m)	0.80	0.80	0.80	0.80
κ	1.70	1.70	1.70	1.70
δ	0.30	0.30	0.30	0.30
B_T (T)	1.77	2.96	1.76	0.97
I_p (MA)	1.78	1.78	1.78	0.97
$\bar{n}_{e,19}$	5.39	4.84	4.36	2.57
Z_{eff}	3.36	3.17	2.53	2.09
P_{aux} (MW)	6.74	10.4	7.40	7.40
$P_{\text{L}\rightarrow\text{H}}$ (MW)	2.57	2.18	3.32	2.84
E_{NBI} (keV)	160.0	160.0	140.0	98.3
$P_{\text{heat}}/(\bar{n}_{e,19}V)$	0.021	0.036	0.028	0.042
$n_{e,19,\text{ped}}^{\text{exp}}$	3.83	4.21	3.36	1.91
$T_{e,\text{ped}}^{\text{exp}}$ (keV)	1.47	1.26	1.05	0.80
$T_{i,\text{ped}}^{\text{exp}}$ (keV)	1.19	1.36	1.28	0.87
$n_{e,19,\text{ped}}^{\text{sim}}$	3.82	3.06	3.14	1.69
$T_{\text{ped}}^{\text{sim}}$ (keV)	1.28	1.55	1.37	0.77
t_{diag} (s)	60.6	60.84	62.9	69.6

B. DIII-D discharges

The 13 DIII-D H-mode discharges include of a ρ_* scan, a β scan, a density scan, a power scan, two pairs of elongation (κ) scans and a high performance discharge. Plasma parameters for these discharges taken from the International Profile Database are listed in Tables V and VI.

Discharges 77557 and 77559 represent a power scan in which the heating power was varied while the average plasma density was held constant.[25] A power balance analysis of these discharges indicates that both electron and ion diffusivities increase with increasing temperature. Discharges 81321 and 81329 represent a density scan at constant temperature. A power balance analysis of these discharges indicates that both the electron and ion diffusivities are independent of the density.[14,25]

Discharges 82205 and 82788, which were part of a DIII-D ρ_* scan, were designed to have the same plasma shape as well the same beta, collisionality, and safety factor as ITER. An analysis of the heat transport in these discharges found that the electron and ion diffusivities and the thermal confinement time scales approximately gyro-Bohm like.[26]

The two pairs of elongation scans, discharges 81499–81507 and 82183–82188, were conducted to test predictions of improved fusion performance at higher elongation. In these scans, it was observed[27] that temperature increases with elongation while other parameters (density, safety factor, heating power) are held fixed. In the β scan, discharges 90117 and 90108, β was varied while the ρ_*, ν_*, and q, were keep constant. A slightly favorable beta scaling of the confinement time was found in this scan.[28]

IV. SIMULATION RESULTS

BALDUR integrated modeling simulations were carried out for the 33 H-mode discharges described in the previous section, using a combination of the pedestal model together with the MMM95 core transport model. Statistical analyses of the simulation results compared with experimental data are described in Sec. IV A. The sensitivity of the simulation results to variations in the pedestal model are presented in Sec. IV B. Trends in the simulation results relative to the experimental data are discussed in Sec. IV C.

A. Statistical analysis

For each of the profiles (ion temperature, electron temperature, and electron density), the normalized deviation, ϵ_j, between the jth experimental data point X_j^{exp} and the simulation result $X^{\text{sim}}(R_j)$ at the major radius R_j of the corresponding experimental data point is defined as

$$\epsilon_j \equiv \frac{X^{\text{sim}}(R_j) - X_j^{\text{exp}}}{X_{\text{max}}^{\text{exp}}}. \tag{7}$$

In order to give all the deviations across each profile equal weight, each deviation is normalized by the maximum experimentally measured value for that given profile, $X_{\text{max}}^{\text{exp}}$. (An alternative choice of normalizing each temperature deviation by the local temperature, for example, would magnify deviations near the edge of the plasma, where temperatures are lower.) The rms deviation σ and the offset f

TABLE V. Plasma parameters for the DIII-D power, n_e, ρ_*, and β scan discharges.

Tokamak discharge type	DIII-D 77557 Low Power	DIII-D 77559 High Power	DIII-D 81321 Low n_e	DIII-D 81329 High n_e	DIII-D 82205 Low ρ_*	DIII-D 82788 High ρ_*	DIII-D 90117 Low β	DIII-D 90108 High β	DIII-D 99411 High perf.
R (m)	1.68	1.69	1.69	1.70	1.68	1.68	1.67	1.68	1.66
a (m)	0.60	0.61	0.56	0.58	0.60	0.59	0.58	0.59	0.54
κ	1.85	1.84	1.83	1.83	1.71	1.67	1.80	1.81	1.84
δ	0.33	0.35	0.29	0.36	0.37	0.35	0.27	0.25	0.56
B_T (T)	2.00	2.00	1.98	1.97	1.81	0.95	1.60	1.91	1.63
I_p (MA)	1.00	1.00	0.99	1.00	1.34	0.66	1.13	1.35	1.20
$\bar{n}_{e,19}$	4.88	5.02	2.94	5.35	5.34	2.86	3.15	6.96	4.72
Z_{eff}	1.68	2.21	2.42	1.65	2.13	1.94	2.38	1.83	2.40
P_{NB} (MW)	4.73	13.23	3.49	8.34	5.86	3.25	1.15	5.84	9.16
$P_{\text{L}\rightarrow\text{H}}$ (MW)	1.77	1.78	1.23	1.78	1.76	0.68	1.15	2.13	1.33
$P_{\text{heat}}/(\bar{n}_{e,19}V)$	0.047	0.123	0.065	0.083	0.058	0.063	0.023	0.043	0.111
$n_{e,19,\text{ped}}^{\text{exp}}$	3.22	3.38	2.13	3.38	3.93	2.28	2.32	6.72	3.47
$T_{e,\text{ped}}^{\text{exp}}$ (keV)	0.55	0.57	0.88	0.44	0.83	0.48	0.41	0.49	1.21
$T_{i,\text{ped}}^{\text{exp}}$ (keV)	0.44	0.27	1.32	0.55	0.95	0.57	0.38	0.50	1.69
$n_{e,19,\text{ped}}^{\text{sim}}$	3.59	3.64	2.18	3.81	3.90	2.03	2.43	5.32	3.47
$T_{\text{ped}}^{\text{sim}}$ (keV)	4.00	0.39	0.92	0.46	0.79	0.51	1.00	0.58	1.05
t_{diag} (s)	2.70	2.70	3.90	3.80	3.66	3.54	2.96	3.09	1.8

between the profile resulting from each simulation and the corresponding experimental data is defined as

$$\sigma = \sqrt{\frac{1}{N}\sum_{j=1}^{N}\epsilon_j^2}, \tag{8}$$

and

$$f = \frac{1}{N}\sum_{j=1}^{N}\epsilon_j, \tag{9}$$

where N is the number of experimental data points in a profile.

The normalized rms deviation σ and the offset f are evaluated for each of the three profiles—ion temperature, electron temperature, and electron density—for the discharges considered. The results of the statistical analyses for

TABLE VI. Plasma parameters for the DIII-D elongation scan discharges.

Tokamak discharge type	DIII-D 81499 Low κ	DIII-D 81507 High κ	DIII-D 82188 Low κ	DIII-D 82183 High κ
R (m)	1.69	1.61	1.69	1.60
a (m)	0.61	0.52	0.61	0.52
κ	1.68	1.95	1.65	1.91
δ	0.32	0.29	0.29	0.22
B_T (T)	1.91	1.91	1.57	1.63
I_p (MA)	1.35	1.34	1.33	1.33
$\bar{n}_{e,19}$	4.81	4.90	6.47	6.87
Z_{eff}	2.33	1.93	1.83	1.95
P_{NB} (MW)	5.74	5.71	3.86	3.85
$P_{\text{L}\rightarrow\text{H}}$ (MW)	1.69	1.42	1.81	1.51
$P_{\text{heat}}/(\bar{n}_{e,19}V)$	0.066	0.078	0.035	0.044
$n_{e,19,\text{ped}}^{\text{exp}}$	4.01	3.24	4.97	4.97
$T_{e,\text{ped}}^{\text{exp}}$ (keV)	0.90	1.20	0.41	0.56
$T_{i,\text{ped}}^{\text{exp}}$ (keV)	0.83	1.18	0.48	0.51
$n_{e,19,\text{ped}}^{\text{sim}}$	3.42	3.48	5.09	4.86
$T_{\text{ped}}^{\text{sim}}$ (keV)	0.91	1.15	0.55	0.79
t_{diag} (s)	4.00	3.8	3.775	3.775

simulations using the standard pedestal model (with $C_W = 2.42$) are presented in Figs. 1 and 2. It can be seen in Fig. 1 that the rms deviations vary from discharge to discharge, and from profile to profile, with a minimum of about 4% and a maximum of about 23%. The normalized offsets shown in Fig. 2 vary from about -15% to $+22\%$.

Note that five discharges (JET discharges 33140, 33465, 34340, 35171, and 35174) are labeled with an "∗" in Figs. 1 and 2. Experimental data are not available for ion temperature in these five discharges and, consequently, the ion temperature profiles were set equal to the electron temperature profiles in the International Profile Database. As a result, these discharges were excluded from the average ion temperature rms deviation and offset described below.

The average rms deviation σ_{avg}—averaged over 28 discharges for the ion temperature, and averaged over all 33 discharges for the electron temperature and density profiles—is about 10% for the ion temperature, electron temperature, and electron density profiles. The average offset, f_{avg}, is about 1.5% for the ion temperature profile, 1.0% for the electron temperature profile, and 0.7% for the electron density profile. These average statistics are about the same as the corresponding statistics obtained when profiles from simulations that use experimental data for the temperatures and density at the top of the pedestal are compared with experimental profiles (see Ref. 4).

B. Variation of the pedestal model

In this section, the pedestal model is varied in a systematic way in order to determine the sensitivity of the predicted profiles to changes in the pedestal model. Consider the coefficient C_W that appears in the equation for the pedestal width ($\Delta = C_W \rho s^2$). The value of C_W was determined in Sec. II B by minimizing the logarithmic rms deviation between the predictions of the model [Eq. (3)] and 533 data points for type 1 ELMy H-mode plasmas from the International Pedestal Database version 3.1. With this value, $C_W = 2.42$, ap-
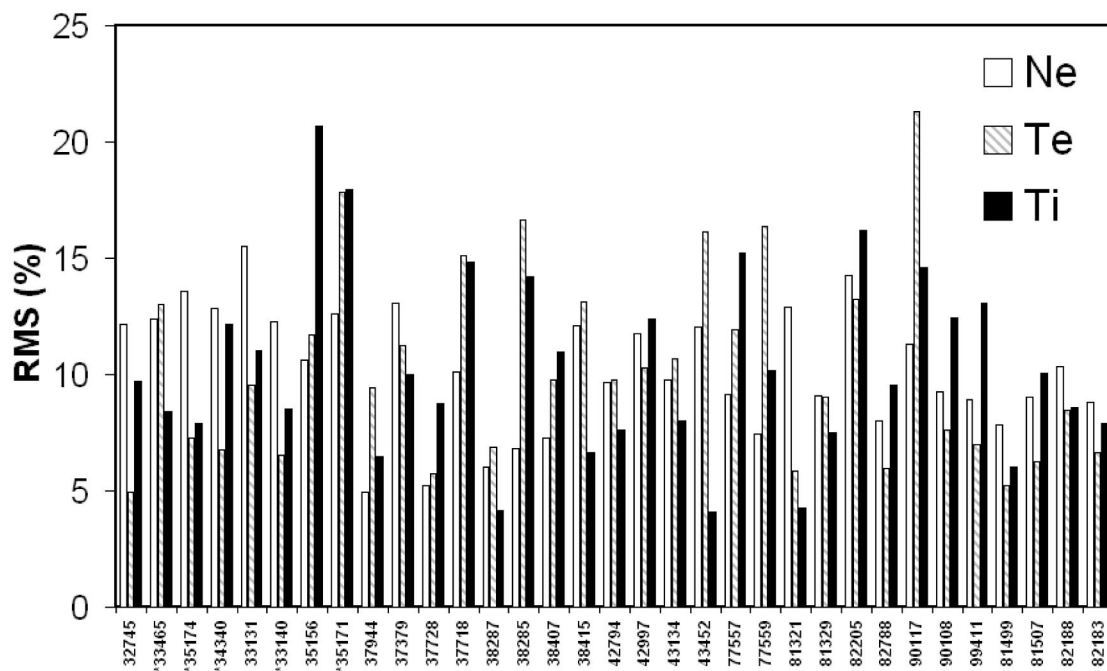
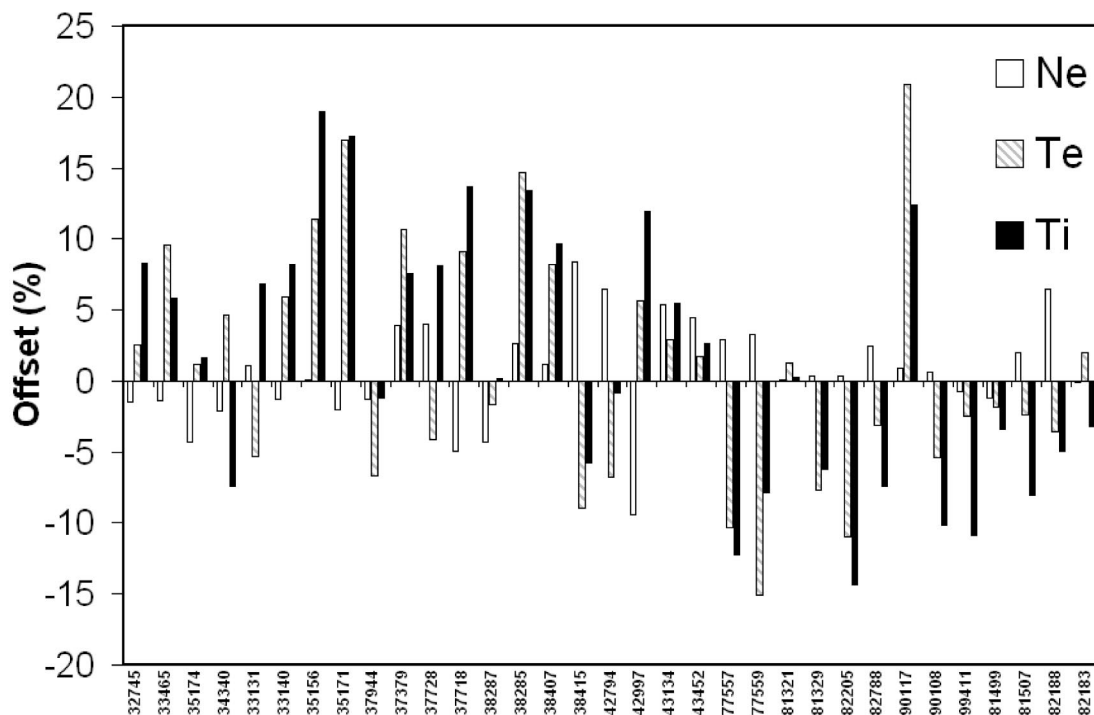FIG. 1. Relative rms deviations (%) for the ion temperature, electron temperature, and density profiles produced by simulations using the MMM95 transport model combined with the standard pedestal model (using $C_W = 2.42$) compared with experimental data for 33 H-mode discharges listed by DIII-D and JET discharge numbers.

proximately half of the data points lie below the model and half lie above the model. The pedestal model with this choice of C_W is referred to as the ''standard model'' in this paper.

If the value of C_W is varied, the fraction of the 533 pedestal temperature data points that lie above and below the model varies, as shown in Fig. 3. As the coefficient C_W is increased from 2.42 to 4.86, the pedestal temperature model sweeps through 34% of the data points above the standard model. Hence, in this paper the pedestal model with $C_W = 4.86$ is referred to as a model that is one standard deviation

FIG. 2. Relative offset from the ion temperature, electron temperature and density profiles produced by simulations using the MMM95 transport model combined with the standard pedestal model (using $C_W = 2.42$) compared with experimental data for 33 H-mode discharges listed by DIII-D and JET discharge numbers.
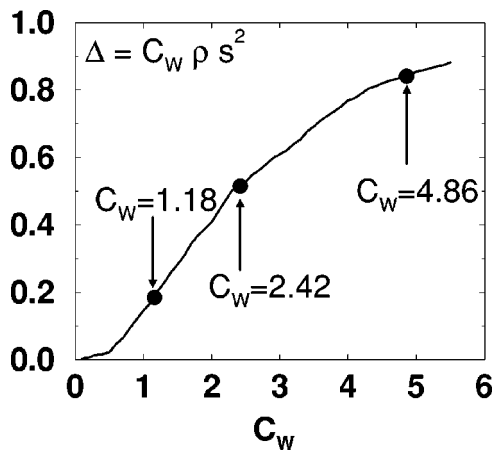
FIG. 3. Fraction of data points for the temperature at the top of the pedestal that lie below the predicted pedestal temperature as a function of the coefficient in the width of the pedestal.
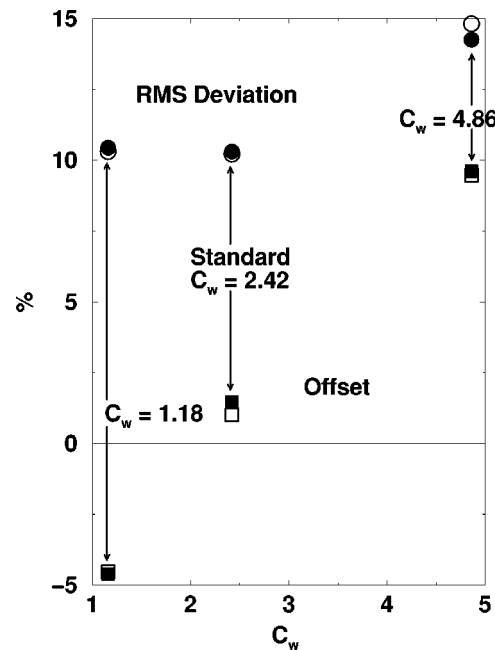

FIG. 4. Relative rms deviation for the ion temperature profiles (solid circles) and electron temperature profiles (open circles), as well as the relative offset for ion temperature profiles (solid squares) and electron temperature profiles (open squares), obtained from simulation profiles compared with experimental data for 33 H-mode discharges, for three values of the coefficient in the width of the pedestal (C_W=1.18, 2.42, and 4.86).

above the standard model, since a standard deviation normally includes approximately 34% of the points within a frequency distribution. Correspondingly, as the coefficient C_W is decreased from 2.42 to 1.18, the pedestal temperature model sweeps through 34% of the data points below the standard model. Hence, in this paper, the pedestal model with C_W=1.18 is referred to as a model that is one standard deviation below the standard model. In determining this range of variation from one standard deviation above to one standard deviation below the standard model, there is no assumption made about the distribution of errors (e.g., no assumption of a Gaussian distribution). In fact, it can be seen in Fig. 3 that the fraction of the data points is not a symmetric function of C_W.

Integrated modeling simulations were carried out for all 33 H-mode discharges using the pedestal model with C_W = 1.18, 2.42, and 4.86. The average rms deviation and offset (as defined in Sec. IV A) for the ion and electron temperature profiles in all 33 H-mode discharges are shown in Fig. 4 for the three values of C_W. The average rms deviation, shown by the points near the top of Fig. 4 varies from about 10% to 15% as the pedestal model is varied over a standard deviation above or below the standard model. It can be seen from the lower points in Fig. 4 that the standard pedestal model (with C_W=2.42) yields an average offset that is less than 1.5% for both the electron and ion temperature profiles, while the pedestal models that are one standard deviation below and above the standard model produce average offsets for the electron and ion temperature profiles that are about -4.5% and $+9.5\%$, respectively. Note that the average offset from the standard pedestal model is small ($<1.5\%$) even though the pedestal and core models were developed independently. That is, the pedestal model was calibrated against 533 data points from the International Pedestal Database while the Multi-Mode core transport model was calibrated against a relatively small number of discharges in 1995 and it has been held fixed since then.

For the density profile, the average rms deviation is approximately 10% and the average offset is less than 1.5%, independent of the model used for the pedestal temperature

width (i.e., simulations using C_W=1.18, 2.42, or 4.86). The statistics for the density profiles are not as important as the statistics for the electron and ion temperature profiles. This is because the electron density profile is relatively tightly constrained by the condition that the average density in the simulation is required to match the average density in the experiment and the shape of the electron density profile is relatively flat in these H-mode plasmas. Given these constraints, the density profile predicted by the simulation cannot differ significantly from the experimental density profile. In contrast, the temperature profiles are not constrained and, so, the comparison between the simulated and experimental temperature profiles provides a more stringent test of the predictive capability of the model than the corresponding comparison of the density profiles.

C. Trends observed in the simulations

A careful inspection of the offsets shown in Fig. 2 revealed that the offsets for the temperature profiles tend to be positive for discharges with low heating power and negative for discharges with high heating power. One way to demonstrate this trend is to plot the offset for each electron and ion temperature profile as a function of the heating power per plasma particle, as shown in Fig. 5, for simulations using the standard pedestal model. In this figure, the horizontal axis indicates the total heating power (MW) divided by the product of the line averaged electron density (in units of 10^{19} particles per m^3) times the plasma volume (approximated by $2\pi^2 R a^2 \kappa$). The vertical axis is the offset, computed from simulations using the standard pedestal model, for the ion temperature profile (shown as open circles for
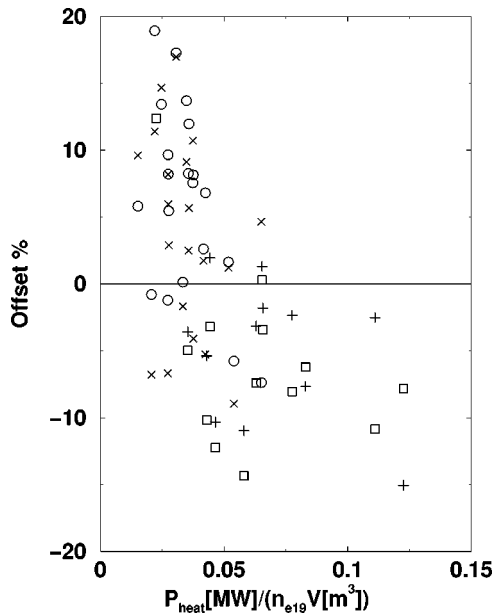
FIG. 5. Offset as a function of heating power (MW) per 10^{19} particles, from simulations using the standard pedestal model (with $C_W=2.42$). Offsets for ion temperature profiles are shown as circles for JET discharges and squares for DIII-D discharges. Offsets for electron temperature profiles are shown as crosses for JET discharges and pluses for DIII-D discharges.
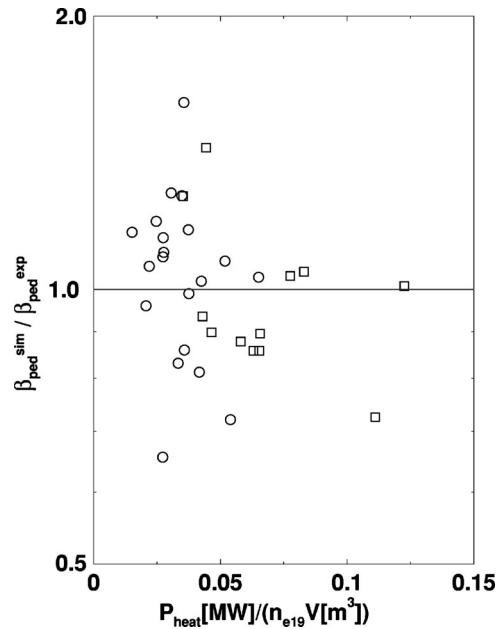
FIG. 6. Ratio of pedestal beta from simulations divided by pedestal beta from experimental data shown for 32 discharges on a logarithmic scale as a function of heating power (MW) per 10^{19} particles. Points from JET discharges are shown as circles while points from DIII-D discharges are shown as squares. One outlier point is omitted.

JET discharges and open squares for DIII-D discharges) and the offset for the electron temperature profile (shown as crosses for JET discharges and pluses for DIII-D discharges). These are the same offsets that are shown in Fig. 2 for the 33 discharges simulated in this paper. It can be seen in Fig. 5 that the temperature profiles tend to be overpredicted (indicated by a positive offset) at low values of the heating power per particle and they tend to be underpredicted (negative offset) at higher values of power per particle. In general, most of the JET discharges (shown as circles and crosses in this figure) have lower power per particle and higher offset than the DIII-D discharges (shown as squares and plusses). It can also be seen in Fig. 5 that the range of offset values (-15% to $+19\%$) is much larger than the average offset ($<1.5\%$) shown in Fig. 4.

Note that burning plasma experiments, such as ITER and FIRE, are expected to have rather low values for the heating power per particle, compared with present-day tokamak experiments.[29] In the ITER design, with $P_{heat}=134$ MW and $\bar{n}_{e,19}=10$, $a=2$ m, $R=6.2$ m, and $\kappa=1.7$, the heating power per particle is $P_{heat}/(n_{e,19}V)=0.016$, in terms of the units used in Fig. 5. For the FIRE design, with $P_{heat}=60$ MW and $\bar{n}_{e,19}=50$, $a=0.6$ m, $R=2.14$ m, and $\kappa=1.76$, the heating power per particle is $P_{heat}/(n_{e,19}V)=0.045$. Even though the heating power is high in these burning plasma experiments, the number of plasma particles is so much larger than in present-day experiments that the power per particle is relatively small. Hence, the simulation protocol used in this paper is likely to overpredict the temperature profiles by about 10% in ITER and by a few percent in the FIRE burning plasma experiment design.

The next issue considered is whether this trend (that the offset decreases as the power per particle increases) is caused primarily by the predictive pedestal model or by the core transport model, or possibly by the two models working together. In an effort to answer this question, the ratio of the simulation pedestal beta to experimentally measured pedestal beta is plotted on a logarithmic scale in Fig. 6 as a function of the heating power per particle (the same variable that is used on the horizontal axis in Fig. 5). One outlier point at $P_{heat}/(nV)=0.023$ and $\beta_{ped}^{sim}/\beta_{ped}^{exp}=2.63$ was omitted from this plot. Note that the prediction of the pedestal relative to experimental data at the pedestal does not have a pronounced trend as a function of the power per particle. Since there is no significant trend in the predictions of the pedestal model compared with experimental data, we conclude that the tendency to overpredict the core temperature profiles at low power per particle is produced more by the core transport model than by the pedestal model.

The rms deviation for β_{ped}—that is $\Sigma(\beta_{ped}^{sim}/\beta_{ped}^{exp}-1)^2/N$—is about 4.2% (with the outlier point removed). Since the predicted pedestal temperature is inversely related to the pedestal density, it turns out that the pedestal pressure and β_{ped}^{sim} are insensitive to the pedestal density. However, the choice of pedestal density does matter when computing the pedestal temperature. If the predicted pedestal density is used, then the rms deviation for the predicted pedestal temperature is about 3.5% (with the outlier point removed). If the experimentally measured pedestal density is used, then the rms deviation for the predicted pedestal temperature is about 1.6% for the discharges considered in this paper. Even though the error is less when the experimentally measured pedestal density is used, a model is needed in which both the density and the temperature are predicted in the pedestal.

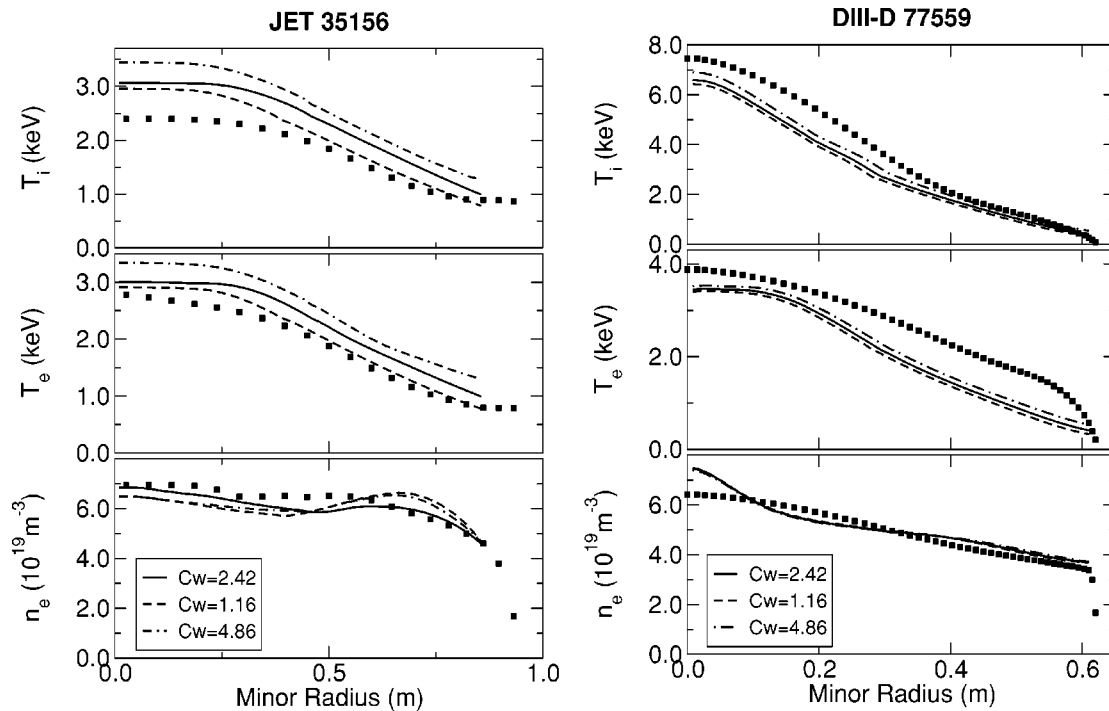Increasing the stiffness of the model would probably

FIG. 7. Profiles for ion temperature (top), electron temperature (middle), and electron density (bottom) are shown as a function of minor radius for the low power per particle JET discharge 35156 (left) and the high power per particle DIII-D discharge 77559 (right). In each panel, dots represent experimental data, while the results are shown for simulations using the standard model (solid curves), one standard deviation above the standard model (dotted–dashed curves), and one standard deviation below the standard model (dashed curves).

make the trend in the offset as a function of power per particle worse because the temperature profiles would be less responsive to the power per particle. Suppose, for example, that the stiffness of the model were increased in a given simulation. At high power per particle, the simulated temperature profile would decrease with increasing stiffness. Hence, the negative offsets at high power per particle in Fig. 5 would become more negative as the stiffness of the model were increased.

It is possible that the omission of flow shear in these simulations might be responsible for the observed trend in the offset as a function of power per particle. Since all the neutral beam injection (NBI) is in the same direction (either co or counter) in the JET and DIII-D tokamaks, and since the toroidal momentum source rate in the plasma is roughly proportional to the NBI power per particle, it would be expected that flow shear would be larger in discharges with high power per particle and smaller in discharges with low power per particle. Hence, flow shear effects would be expected to reduce transport to a greater extent and, therefore, to increase the temperature and to increase the offset in discharges with high power per particle.

D. Profile shapes

Profiles are shown in Fig. 7 from simulations using the three variations of the pedestal model compared with experimental data for a discharge with low heating power per particle (JET discharge 35156) and a discharge with high heating power per particle (DIII-D discharge 77559). It can be seen that the simulation profiles for electron and ion tem-

perature using the standard model (solid curve in the top two panels on each side) are systematically higher than (overpredicts) the experimental data (represented by dots in Fig. 7) for the low heating power per particle discharge 35156 and systematically lower than (underpredicts) the experimental data for the high heating power per particle discharge 77559. These results are consistent with the trend described in the last section of a positive offset (simulation profile higher than experimental data) for discharges with low heating power per particle and a negative offset (simulation profile lower than experimental data) for discharges with high heating power per particle. As shown in Fig. 7, the conditions at the boundary of the simulations that used the standard pedestal model (at the right edge of the solid curve in each panel) nearly match the corresponding experimental data. Consequently, the differences between the simulated profiles and the experimental data are the result of the core models used in the simulations—either the core transport model or the models used for sources and sinks.

Simulations using the pedestal models that are one standard deviation above and below the standard pedestal model are also shown in Fig. 7. It can be seen that the temperature profiles shift nearly rigidly up and down as the pedestal model is changed from the standard model (solid curve) to one standard deviation above (dotted–dashed curve) and below (dashed curve) the standard pedestal model. The difference between the predicted profiles is more pronounced in the discharge with low heating power per particle. The density profiles resulting from these simulations (bottom panels) remain nearly unchanged as the pedestal temperature model

is changed, since the pedestal density model remains the same in all the simulations.

The central ion temperature is considerably higher than the central electron temperature in the discharge with high heating power per particle (discharge 77559 on the right-hand side of Fig. 7) while the central electron and ion temperatures are more nearly the same in the discharge with low heating power per particle (discharge 35156 on the left-hand side of Fig. 7). This is true for the temperature profiles predicted by the simulations, as well as the corresponding experimentally measured temperature profiles. In general, the discharges with high heating power per particle were found to have central ion temperatures higher than central electron temperatures, while the discharges with low heating power per particle were found to have central electron and ion temperatures that were nearly equal. This is significant because it is known that the growth rate of the ion temperature gradient (ITG) mode and the resulting transport driven by the ITG mode are reduced as T_i/T_e is increased.[7] Since the ITG mode is the dominant contribution to the Multi-Mode transport model in the core of the plasma, the increase in T_i/T_e causes a reduction in transport and an increase in both temperatures.

The central ion temperature is larger than the central electron temperature in discharges with high power per particle discharges because the ion heating power is larger than the electron heating in those discharges. The physical reasons for this trend can be understood in the following way. First, the Ohmic heating power, which is almost entirely to the electrons, becomes less significant as the auxiliary heating power is increased. The second reason has to do with the way NBI heating is affected by the electron temperature, which can be described in the following way: Each fast ion produced by neutral beam injection transfers most of its energy to thermal electrons until it slows down below a critical energy, after which it transfers most of its energy to thermal ions.[30] That critical energy increases with increasing electron temperature, which, in turn, increases with increasing heating power per particle. Since the initial energy of the NBI fast ions is independent of the NBI heating power, the gap between the initial fast ion energy and the critical energy decreases as the critical energy increases. Hence, increasing the heating power has the effect of increasing both the electron and ion temperature, which increases the critical energy, which decreases the gap between the initial NBI fast ion energy and the critical energy, which increases the fraction of power transferred to the thermal ions, which increases the ion temperature over the electron temperature.

Finally, the profiles normalized by their central values are shown in Fig. 8 for the same two discharges that are shown in Fig. 7. It can be seen from the normalized profiles in Fig. 8 that the temperature and density profiles are more peaked in the discharge with high heating power per particle. There are several possible causes for this profile peaking. For example, the NBI power deposition profile is somewhat more peaked in the simulations of discharges with higher power per particle. In particular, the half width of the NBI deposition profile divided by the minor radius changes from 0.70 in the discharge with low power per particle to 0.55 in
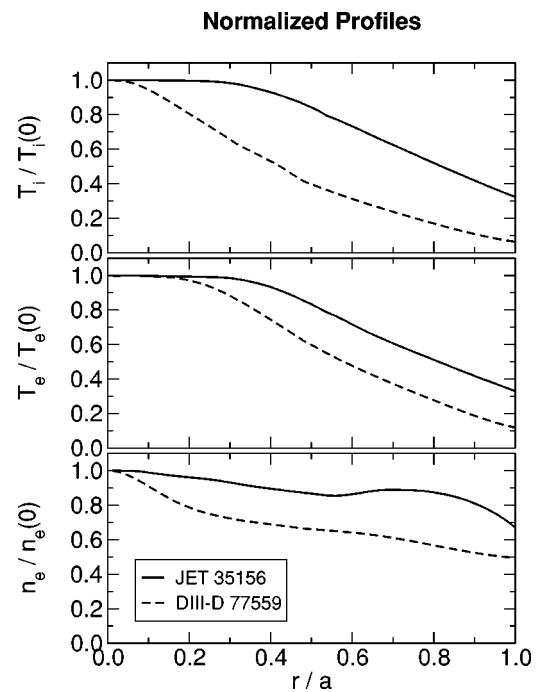

Normalized Profiles

FIG. 8. Normalized profiles for ion temperature (top), electron temperature (middle), and electron density (bottom) are shown as a function of normalized minor radius for the low power per particle JET discharge 35156 (solid lines) and the high power per particle DIII-D discharge 77559 (dashed lines).

the discharge with high power per particle. This change in the shape of the power deposition profile, however, could at least partly be a response to the temperature and density peaking, rather than the main cause.

Another significant difference that was found between the two discharges is the shape of the thermal diffusivity profile for each discharge. The normalized half width of the ion thermal diffusivity profile changes from 0.53 in the low power per particle discharge to 0.83 in the high power per particle discharge. This change in the shape of the diffusivity profile is consistent with the observation that the growth rate of the ITG mode decreases as T_i/T_e increases. Hence, the sequence of physical effects can be understood in the following way: As the power per particle is increased from one discharge to another, the fraction of the power to the ions increases over the fraction of the power to the electrons. This causes the central ion temperature to become larger than the central electron temperature, which, in turn, causes the thermal and particle transport driven by the ITG mode in the deep core of the plasma to decrease relative to the transport near the edge of the plasma. As a result, the temperature and density profiles become more peaked.

V. CONCLUSIONS

In this paper, an integrated modeling protocol is used to predict the temperature and density profiles in H-mode plasmas and to compare those profiles with experimental data from 33 discharges in the JET and DIII-D tokamaks. The protocol consists of the following parts: A pedestal model is used to predict the temperature and density at the top of the

pedestal at the edge of the simulations, together with models to compute the core thermal and particle transport, all the heat and particle sources and sinks, the current profile, the shapes of the magnetic flux surfaces within the plasma, and the effects of large scale instabilities, such as sawtooth oscillations. These models are used in the BALDUR code to predict the time evolution of the temperature, density, and other plasma profiles. A systematic procedure is then used to set up input data and to run the BALDUR code for all the discharges. Finally, a systematic procedure is used to compare the results of the simulations with experimental data and to compute statistics that quantify the comparisons.

When the results of the simulations using this protocol are compared with experimental data from 33 JET and DIII-D H-mode discharges, it is found that the average relative rms deviation is approximately 10% and the average relative offset is approximately 1% for the ion temperature, electron temperature, and electron density profiles. When the experimentally measured profiles are compared with the profiles computed using this protocol, the agreement is as good as the agreement obtained when experimental data is used to provide the boundary conditions for the simulations,[4] rather than a predictive pedestal model. If the pedestal model is varied over one standard deviation below and above the standard model, it is found that the average relative offset for the profiles varies from about −5% to +9%.

It is found that there is a systematic trend in the offset as a function of the heating power per plasma particle. The simulations systematically over-predict the temperature profiles, with an average offset of about +10%, at the lowest values of heating power per particle, while the simulations systematically underpredict the temperature profiles, with an average offset of about −10%, at the highest values of heating power per particle. It is found that the core models for transport and sources are responsible for this systematic trend in the error.

With the exception of the impurity concentration at the edge of the plasma, all of the input data used in these integrated modeling simulations are parameters that are under the control of the experimentalists (such as plasma current, magnetic field strength, plasma shape, heating power, and average plasma density). As a result, this protocol provides a tool that can be used to predict the temperature and density profiles in new experiments. These predictions are needed in order to better understand the physics of confinement in tokamaks and to predict the performance of burning plasma experiments such as ITER or FIRE.

[1] F. Wagner, G. Becker, K. Behringer *et al.*, Phys. Rev. Lett. **49**, 1408 (1982).
[2] T. H. Osborne *et al.*, in *Proceedings of the Twenty-Fourth European Conference on Controlled Fusion and Plasma Physics* (European Physical Society, Berchtesgaden, Germany, 1997).
[3] M. Greenwald, R. Boivin, F. Bombarda *et al.*, Nucl. Fusion **37**, 793 (1997).
[4] D. Hannum, G. Bateman, J. Kinsey, A. H. Kritz, T. Onjun, and A. Pankin, Phys. Plasmas **8**, 964 (2001).
[5] J. E. Kinsey, Nucl. Fusion **39**, 539 (1999).
[6] T. Onjun, G. Bateman, A. H. Kritz, and G. Hammett, Phys. Plasmas **9**, 5018 (2002).
[7] G. Bateman, A. H. Kritz, J. E. Kinsey, A. J. Redd, and J. Weiland, Phys. Plasmas **5**, 1793 (1998).
[8] C. E. Singer, D. E. Post, D. R. Mikkelsen *et al.*, Comput. Phys. Commun. **49**, 275 (1988).
[9] J. E. Kinsey and G. Bateman, Phys. Plasmas **3**, 3344 (1996).
[10] T. Onjun, G. Bateman, A. H. Kritz, and D. Hannum, Phys. Plasmas **8**, 975 (2001).
[11] G. Bateman, A. H. Kritz, V. V. Parail *et al.*, Phys. Plasmas **6**, 4607 (1999).
[12] V. Parail, G. Bateman, M. Becoulet *et al.*, Plasma Phys. Rep. **29**, 539 (2003).
[13] G. W. Pacher, H. D. Pacher, A. S. Kukushkin, G. Janeschitz, and G. Pereverzev, Nucl. Fusion **43**, 188 (2003).
[14] D. Boucher, J. Connor, W. Houlberg *et al.*, Nucl. Fusion **40**, 1955 (2000).
[15] P.-H. Rebut, R. J. Bickerton, and B. E. Keen, Nucl. Fusion **25**, 1011 (1985).
[16] J. L. Luxon and L. G. Davis, Fusion Technol. **8**, 441 (1985).
[17] A. H. Kritz, G. Bateman, T. Onjun, A. Pankin, and C. Nguyen, in *Proceedings of the European Physical Society Meeting*, Montreux, Switzerland, June 2002 (European Physical Society, Petit-Lancy, Switzerland, 2002).
[18] Y. Shimomura, R. Aymar, V. Chuyanov *et al.*, in *Proceedings of the Eighteenth International Atomic Energy Agency Fusion Energy Conference*, Sorrento, Italy, 4–10 October 2000 (International Atomic Energy Agency, Vienna, 2001).
[19] J. G. Cordey, B. Balet, D. V. Bartlett *et al.*, Nucl. Fusion **39**, 301 (1999).
[20] B. Balet *et al.*, in *Proceedings of the 22nd European Conference*, Bournemouth, 1995 (European Physical Society, Geneva, 1995), Vol. 19C, p. 935, Part I.
[21] J. G. Cordey, B. Balet, D. Campbell *et al.*, Plasma Phys. Controlled Fusion **38**, A67 (1996).
[22] S. M. Kaye and the ITER Confinement Database and Modeling Group, in *Proceedings of the 15th International Conference*, Seville, 1994 (International Atomic Energy Agency, Vienna, 1995), Vol. 2, p. 525.
[23] G. Matthews, S. Allen, N. Asakura *et al.*, J. Nucl. Mater. **241–243**, 450 (1997).
[24] D. J. Campbell, A. Bickley, A. Chankin *et al.*, Plasma Phys. Controlled Fusion **38**, 1497 (1996).
[25] D. Schissel, Plasma Phys. Controlled Fusion **38**, 1487 (1996).
[26] C. C. Petty, T. Luce, K. Burrell *et al.*, Phys. Plasmas **2**, 2342 (1995).
[27] C. M. Greenfield, J. C. DeBoo, T. H. Osborne, F. W. Perkins, M. N. Rosenbluth, and D. Boucher, Nucl. Fusion **37**, 1215 (1997).
[28] C. C. Petty, T. Luce, J. DeBoo *et al.*, Nucl. Fusion **38**, 1183 (1998).
[29] G. Bateman, T. Onjun, and A. H. Kritz, ''Integrated predictive modeling simulations of burning plasma experiment designs,'' Plasma Phys. Controlled Fusion (to be published).
[30] J. Wesson and D. J. Campbell, *Tokamaks* (Clarendon, Oxford, 1997).